In-duct flow computation and acoustic propagation using the admittance multimodal formulation

Bruno Mangin, Gwenael Gabard, Majd Daroukh

In-duct flow computation and acoustic propagation using the admittance multimodal formulation

B. Mangin[a],[1,2] G. Gabard,[1] and M. Daroukh[2]

[1] *Laboratoire d'Acoustique de l'Université du Mans (LAUM), UMR 6613, Institut d'Acoustique - Graduate School (IA-GS), CNRS, Le Mans Université, France*

[2] *Department of Aerodynamics, Aeroelasticity, and Aeroacoustics (DAAA), ONERA, Institut Polytechnique de Paris, 92320 Châtillon, France*

(Dated: 28 May 2024)

[a] bruno.mangin@safrangroup.com

A multimodal method for computing the potential base flow and propagating acoustic perturbations inside axisymmetric ducts is presented. Instead of using the standard modal basis, a polynomial basis is used in the radial direction to reduce the computational cost of the method, but this introduces non-physical high-order modes. The impact of these modes on the stability of the calculation is examined, and for the acoustic computation, a modification of the axial integration is proposed to improve the conditioning of the matrices involved. The flow computation is achieved by applying the method (initially devoted to acoustics) at a zero frequency without convective effects, by modifying the definition of the admittance at the exit of the duct and by performing an induction process on the density. The method is validated against a finite element method for ducts with hard walls or lined walls. The results show that the proposed multimodal method is very efficient in computing the mean flow and propagating the sound disturbances inside axisymmetric ducts.

I. INTRODUCTION

The accurate prediction of sound wave propagation in ducts is a crucial challenge in turbofan engineering, and various methods are employed when a mean flow is present. These methods can be broadly classified as numerical or semi-analytical/semi-numerical. Numerical methods, such as finite difference 1–3 and finite element 4–7, are versatile and can accommodate general geometries and mean flow profiles. Still, they are computationally expensive as they do not take advantage of the ducted aspect of the problem. In contrast, semi-analytic methods, such as WKB 8–10, pseudo-spectral 11 or multimodal 12–16, can be fast, but they face difficulties in handling irregular geometry or non-uniform mean flow. These methods are based on the idea of dissociating the propagation in the axial direction from the acoustic shape in the transverse direction. Until recently, multimodal methods were limited to cases with no flow or with a uniform flow 12–14, but a recent extension to account for a multiple-scale flow has been proposed 16. Even if this method appeared promising for low frequencies and Mach numbers, the results became less accurate for high Mach numbers because of the multiple-scale approximation of the flow.

This work therefore aims to extend the multimodal methodology to account for an accurate flow description. As for the previous studies, the method is intended to compute the acoustic field in the presence of an already-known base flow (the novelty being here that it can be heterogeneous as long as it remains potential). But in order to obtain fast predictions on the whole, the multimodal method is here also used to compute the base flow by analogy with an acoustic field at a zero frequency and without convective effects. In the proposed

method, Chebyshev polynomials are used to represent the acoustics in the radial direction. The polynomial basis offers excellent convergence properties for smooth geometries. However, as this basis is non-physical, high-order modes (not well captured by the polynomial basis) are present in the calculation and must be handled with care 17, 18. Here the authors propose to modify the Magnus–Möbius scheme 14, 19 traditionally used for the axial computation. This modification is based on an eigendecomposition of the Magnus matrix. The involved matrices are then rewritten to avoid the summation of high values associated with right-running non-physical eigenmodes with low values associated with left-running non-physical eigenmodes. To validate our method for axisymmetric cases, we compare it to the classical finite element method (FEM), which is commonly used for predicting sound wave propagation in ducts. We focus on the accuracy and stability of our predictions for various modes and frequencies.

The paper is organized as follows. Section II provides a brief overview of the equations governing the flow and acoustic fields, which serve as a basis for constructing the proposed formulation. Section III describes the developed multimodal method for computing the acoustic field in the presence of a heterogeneous potential flow (supposed to be known at this step), and section IV details the adaptation of the method for computing the aforementioned potential flow. The developed method is then validated against a FEM code in section V for a realistic engine geometry with hard walls and lined walls. Conclusions and discussions are finally provided in section VI.

II. GOVERNING EQUATIONS

In this work, we study the linear propagation of sound in a waveguide with an axially varying circular or annular cross-section, defined by the inner and outer radii R_1 and R_2. The analysis is performed in the frequency domain, with ω the angular frequency, and all the variables are dimensionless (see Reference 8 for more details). We express the velocity vector, density and speed of sound variables as follows

$$\begin{aligned} \tilde{\mathbf{v}} &= \mathbf{V} + \mathrm{Re}(\mathbf{v}\ \mathrm{e}^{\mathrm{i}\omega t}) = (U, V, W) + \mathrm{Re}((u, v, w)\ \mathrm{e}^{\mathrm{i}\omega t}), \\ \tilde{\rho} &= D + \mathrm{Re}(\rho\ \mathrm{e}^{\mathrm{i}\omega t}), \\ \tilde{c} &= C + \mathrm{Re}(c\ \mathrm{e}^{\mathrm{i}\omega t}). \end{aligned} \tag{1}$$

Capital letters denote time-averaged quantities, and lower-case letters represent unsteady harmonic perturbations.

The flow is assumed to be a potential perfect gas flow. Therefore, the mean flow velocity and the acoustic velocity derive from scalar potentials, denoted Φ and ϕ, respectively. The equations for the mean flow and the perturbations may be written

$$\nabla \cdot (D \nabla \Phi) = 0, \tag{2a}$$

$$\frac{D^{\gamma-1}}{\gamma - 1} + \frac{1}{2} \nabla \Phi \cdot \nabla \Phi = E, \tag{2b}$$

$$\nabla \cdot (D \nabla \phi) - D \frac{\mathrm{D}}{\mathrm{D}t} \left(\frac{1}{C^2} \frac{\mathrm{D}\phi}{\mathrm{D}t} \right) = 0, \tag{2c}$$

$$p = -D \frac{\mathrm{D}\phi}{\mathrm{D}t}, \tag{2d}$$

with $\mathrm{D}/\mathrm{D}t = \mathrm{i}\omega + \mathbf{V} \cdot \nabla$ the convective derivative, $\mathbf{V} = \nabla\Phi$, $\mathbf{v} = \nabla\phi$ and where γ is the ratio of specific heats and E a Bernoulli constant. The walls of the duct are impermeable

to the mean flow

$$\mathbf{V} \cdot \mathbf{n} = 0. \tag{3}$$

The duct walls can be acoustically lined, using a locally reacting treatment. The Ingard–Myers impedance condition is used for this purpose [20]

$$\mathrm{i}\omega \nabla\phi \cdot \mathbf{n} = -\left[\frac{\mathrm{D}}{\mathrm{D}t} - \mathbf{n} \cdot (\mathbf{n} \cdot \nabla \mathbf{V})\right] \left(\frac{D}{Z}\frac{\mathrm{D}\phi}{\mathrm{D}t}\right), \tag{4}$$

with $\mathbf{n}$ the unit outgoing vector normal to the surface and Z the local impedance of the liner.

To apply the multimodal method, the governing equation must be rearranged into a system with only first-order derivatives in the axial direction x. The chosen variables are the acoustic potential ϕ and its axial derivative u. The system then becomes

$$\frac{\partial \phi}{\partial x} = u, \tag{5a}$$

$$D\frac{\partial}{\partial x}\left(\left(1 - M_x^2\right) u\right) = D\frac{\mathrm{D}}{\mathrm{D}t}\left(\frac{1}{C^2}\frac{\mathrm{D}_\perp \phi}{\mathrm{D}t}\right) + D\frac{\mathrm{D}_\perp}{\mathrm{D}t}\left(\frac{Uu}{C^2}\right) + \frac{D}{2C^2}\frac{\partial}{\partial x}\left(\mathbf{V}_\perp \cdot \mathbf{V}_\perp\right) u - \nabla_\perp \cdot (D\nabla_\perp \phi), \tag{5b}$$

in which $M_x = U/C$ is the axial Mach number. The symbol $\perp$ refers to the transverse direction, so that $\nabla_\perp$ is the gradient operator restricted to the cross-section. In addition, $\mathbf{V}_\perp$ is the mean flow velocity along the duct cross-section, and $\mathrm{D}_\perp/\mathrm{D}t = \mathrm{i}\omega + \mathbf{V}_\perp \cdot \nabla$.

III. MULTIMODAL FORMULATION FOR THE ACOUSTIC FIELD

This section presents the formulation of a multimodal method to solve the model described above, assuming that the mean flow is known.

A. Variational formulation

The weak formulation of equations (5a) and (5b) is obtained by multiplying them by the complex conjugate of a test function g and by integrating over the duct cross-section, denoted S, whose boundary is the contour Λ. After some manipulations, one can write

$$\int_S D(1-M_x^2)\frac{\partial \phi}{\partial x}g^* \mathrm{d}S = \int_S D(1-M_x^2)ug^* \mathrm{d}S, \tag{6a}$$

$$\begin{aligned}\frac{\mathrm{d}}{\mathrm{d}x}\left(\int_S D(1-M_x^2)ug^* - \frac{DU}{C^2}\frac{\mathrm{D}_\perp \phi}{\mathrm{D}t}g^* \mathrm{d}S\right) = \int_S D(1-M_x^2)u\frac{\partial g^*}{\partial x} + D\nabla_\perp g^* \cdot \nabla_\perp \phi \\ - \frac{D}{C^2}\left(\frac{\mathrm{D}_\perp \phi}{\mathrm{D}t}\left(\frac{\mathrm{D}_\perp g}{\mathrm{D}t}\right)^* + Uu\left(\frac{\mathrm{D}_\perp g}{\mathrm{D}t}\right)^* + U\frac{\mathrm{D}_\perp \phi}{\mathrm{D}t}\frac{\partial g^*}{\partial x}\right)\mathrm{d}S - \int_\Lambda Dg^* \nabla \phi \cdot \mathbf{n}\mathrm{d}\Lambda.\end{aligned} \tag{6b}$$

in which $*$ denotes the complex conjugate.

The impedance condition (4) is used for the last term in (6b). Following Eversmann 21, we use Stokes' theorem to rewrite this term as follows

$$\begin{aligned}\int_\Lambda Dg^* \nabla \phi \cdot \mathbf{n}\ \mathrm{d}\Lambda = \frac{1}{\mathrm{i}\omega}\int_\Lambda \frac{D^2}{Z}\left(Uu\left(\frac{\mathrm{D}g}{\mathrm{D}t}\right)^* + \frac{\mathrm{D}_\perp \phi}{\mathrm{D}t}\left(\frac{\mathrm{D}g}{\mathrm{D}t}\right)^*\right)\ \mathrm{d}\Lambda - \\ \frac{1}{\mathrm{i}\omega}\frac{\mathrm{d}}{\mathrm{d}x}\left[\int_\Lambda \frac{D^2}{Z}\left(Uu + \frac{\mathrm{D}_\perp \phi}{\mathrm{D}t}\right)g^*(\mathbf{V}\cdot\boldsymbol{\tau})\mathrm{d}\Lambda\right],\end{aligned} \tag{7}$$

where $\boldsymbol{\tau}$ is the unit vector tangential to the duct wall. In the remainder of the paper, $\mathbf{V}\cdot\boldsymbol{\tau}$ is simply denoted V_τ. In the special case of a circular duct ($R_1 = 0$), the last term in (6b) vanishes on the inner duct wall since $\mathrm{d}\Lambda_1 = R_1 \mathrm{d}\theta = 0$.

B. Modal decomposition

To apply the multimodal method, the governing equation (6) must be rearranged into a system with only first-order derivatives in the axial direction x. To that end, the cho-

sen variables are the acoustic potential ϕ and its axial derivative $u = \partial\phi/\partial x$. They are represented using a set of linearly independent transverse cross-section functions, denoted $(\varphi_j)_{j\in\mathbb{N}}$. Using this basis, the acoustic potential and its axial derivative are written

$$\phi = \sum_j \phi_j(x)\varphi_j(x,r,\theta)\ , \quad \text{and } u = \sum_j u_j(x)\varphi_j(x,r,\theta). \tag{8}$$

The same basis is used for the test functions associated to ϕ and u. The equations (6) and (7) then become

$$\int_S D(1-M_x^2)\varphi_i^*\varphi_j \mathrm{d}S\frac{\mathrm{d}\phi_j}{\mathrm{d}x} = -\int_S D(1-M_x^2)\varphi_i^*\frac{\partial\varphi_j}{\partial x}\mathrm{d}S\phi_j + \int_S D(1-M_x^2)\varphi_i^*\varphi_j\mathrm{d}Su_j,$$

$$\begin{aligned}
&\frac{\mathrm{d}}{\mathrm{d}x}\left(\int_S D(1-M_x^2)\varphi_j\varphi_i^*\mathrm{d}Su_j - \int_S \frac{DU}{C^2}\frac{\mathrm{D}_\perp\varphi_j}{\mathrm{D}t}\varphi_i^*\mathrm{d}S\phi_j\right) = \\
&+\left(\int_S D\nabla_\perp\varphi_i^*\cdot\nabla_\perp\varphi_j - \frac{D}{C^2}\frac{\mathrm{D}_\perp\varphi_j}{\mathrm{D}t}\left(\frac{\mathrm{D}\varphi_i}{\mathrm{D}t}\right)^*\mathrm{d}S - \frac{1}{\mathrm{i}\omega}\int_\Lambda \frac{D^2}{Z}\frac{\mathrm{D}_\perp\varphi_j}{\mathrm{D}t}\left(\frac{\mathrm{D}\varphi_i}{\mathrm{D}t}\right)^*\mathrm{d}\Lambda\right)\phi_j \\
&+\left(\int_S D(1-M_x^2)\varphi_j\frac{\partial\varphi_i^*}{\partial x} - \frac{DU}{C^2}\varphi_j\left(\frac{\mathrm{D}_\perp\varphi_i}{\mathrm{D}t}\right)^*\mathrm{d}S - \frac{1}{\mathrm{i}\omega}\int_\Lambda\frac{D^2U}{Z}\varphi_j\left(\frac{\mathrm{D}\varphi_i}{\mathrm{D}t}\right)^*\mathrm{d}\Lambda\right)u_j \\
&+\frac{1}{\mathrm{i}\omega}\frac{\mathrm{d}}{\mathrm{d}x}\left(\int_\Lambda\frac{D^2V_\tau}{Z}\frac{\mathrm{D}_\perp\varphi_j}{\mathrm{D}t}\varphi_i^*\mathrm{d}\Lambda\phi_j + \int_\Lambda\frac{D^2V_\tau U}{Z}U\varphi_j\varphi_i^*\mathrm{d}\Lambda u_j\right).
\end{aligned} \tag{9}$$

These expressions can be written in vector form by introducing the vectors $\boldsymbol{\phi}$ and $\mathbf{u}$ containing the unknowns $\phi_j(x)$ and $u_j(x)$. The equations governing the axial variation of these vectors are

$$\begin{pmatrix} A_{11} & A_{12} \\ A_{21} & A_{22} \end{pmatrix}\frac{\mathrm{d}}{\mathrm{d}x}\begin{pmatrix}\boldsymbol{\phi}\\ \mathbf{u}\end{pmatrix} = \begin{pmatrix} M_{11} & M_{12} \\ M_{21} & M_{22} \end{pmatrix}\begin{pmatrix}\boldsymbol{\phi}\\ \mathbf{u}\end{pmatrix}. \tag{10}$$

The detailed expressions for the matrices A_{11}, A_{12}, A_{21}, A_{22}, M_{11}, M_{12}, M_{21} and M_{22} are given in Appendix A. The two vectors $\boldsymbol{\phi}(x)$ and $\mathbf{u}(x)$ are linked through the admittance matrix Y such that $\mathbf{u}(x) = Y(x)\boldsymbol{\phi}(x)$.

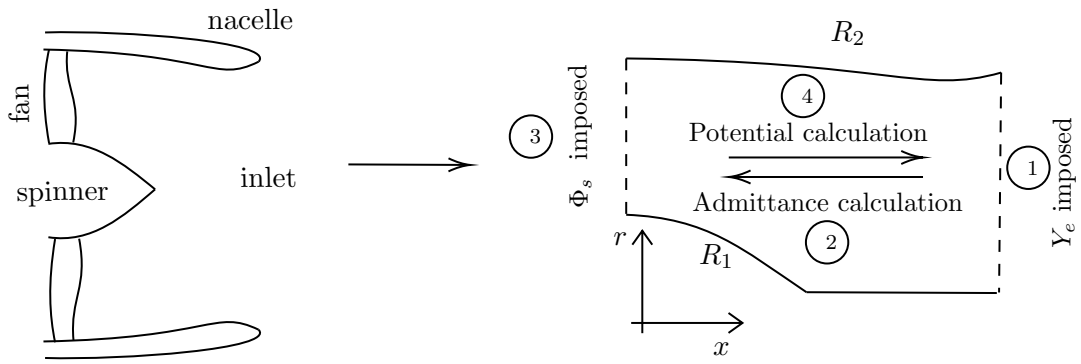

FIG. 1. Schematic of the calculation performed.

C. Overview of the calculation

Before going deeper into the numerical details of the method, an overview of the procedure to perform a multimodal computation is given in the following and is depicted in Figure 1. Let us suppose that we want to compute the acoustic propagation inside the ducted part of an aero-engine. This region is considered to be a duct whose cross-section varies axially. In the following, the source denotes the fan plane location while the exit refers to the inlet plane. First, the admittance Y_e at the exit is imposed. Using this initial value, the admittance Y is calculated from the exit to the source using a Magnus–Möbius scheme. Next, the potential at the source $\mathbf{\Phi}_s$ is calculated using the specified injected wave and the previously obtained admittance. Finally, the Magnus–Möbius scheme is once more employed to obtain the potential throughout the entire engine.

D. Transverse mode basis

In multimodal methods, the basis functions φ_j are generally the local transverse mode of a hard-walled duct (i.e. Fourier-Bessel modes for an axisymmetric duct)[12–14, 22]. However,

these bases tend to yield slow convergence rates, and additional modes are often required to improve the accuracy of the calculations 15, 23. In this paper, we focus on axisymmetric ducts, and therefore, a Fourier transform is used to represent the acoustic field in the circumferential direction. However, Chebyshev functions are preferred in the radial direction since they provide good convergence properties 24–26. As in Reference 16, for each basis function index j, we associate a pair $(m, p) \in (\mathbb{Z}, \mathbb{N})$ such that

$$\varphi_p^m = \left(\frac{r}{R_2 - R_1}\right)^{\min(|m|,1)} T_p\left(\frac{r - R_1}{R_2 - R_1}\right) \mathrm{e}^{-\mathrm{i}m\theta}, \tag{11}$$

where T_p is the shifted Chebyshev polynomial of order p, related to the Chebyshev polynomials T_p^* by the relation $T_p(x) = T_p^*(2x - 1)$. The inclusion of the factor $r^{\min(|m|,1)}$ ensures that all the matrices given in Appendix A are well-defined. This factor is included based on the property of propagating modes, which exhibit a behaviour of r^m as $r \to 0$ 27. Here we use the $\min(|m|, 1)$ exponent so that the multimodal matrices are the same for all non-zero azimuthal wavenumbers. Note that this reduces the number of polynomials needed to represent the acoustic field if the transverse section is circular without increasing it when it is annular.

For the remainder of the paper, the duct is considered axisymmetric, so there is no possible coupling between different circumferential Fourier modes. Therefore we consider that the value of the azimuthal order m is fixed, and, in the rest of the paper, no distinction is made between φ_p^m and φ_p.

E. Admittance calculation

Introducing the definition of the admittance matrix in Equation (10), it is possible to show that this matrix satisfies a Riccati equation of the form

$$\frac{\mathrm{d}Y}{\mathrm{d}x} = -YA_{11}^{-1}M_{11} - YA_{11}^{-1}M_{12}Y - A_{22}^{-1}A_{21}A_{11}^{-1}(M_{11} + M_{12}Y) + A_{22}^{-1}M_{21} + A_{22}^{-1}M_{22}Y \ . \quad (12)$$

This equation is solved numerically using a Magnus–Möbius scheme starting from an initial value Y_e. This numerical procedure is described in detail in References 14 and 19.

We use the same procedure as in References 16, 22 to define the matrix Y_e. We assume an infinite duct termination with constant cross-section with only forward waves. To determine the admittance at the exit, the acoustic variables are expressed as a summation of modes that either propagate or decay exponentially with respect to the axial distance. By doing so, the problem of equation (10) simplifies to the following eigenvalue problem

$$\mathrm{i}\lambda_i \begin{pmatrix} A_{11} & A_{12} \\ A_{21} & A_{22} \end{pmatrix} \begin{pmatrix} \mathbf{w}_i^{\phi} \\ \mathbf{w}_i^{u} \end{pmatrix} = \begin{pmatrix} M_{11} & M_{12} \\ M_{21} & M_{22} \end{pmatrix} \begin{pmatrix} \mathbf{w}_i^{\phi} \\ \mathbf{w}_i^{u} \end{pmatrix}, \quad (13)$$

the solution of which gives the eigenvalues λ_i and the eigenvectors associated with the acoustic potential $\mathbf{w}_i^{\phi}$ and axial velocity $\mathbf{w}_i^{u}$ waves. These waves are separated into the forward (+) and backward (−) directions based on the sign of $\mathrm{Re}(\lambda_i) - \omega/\overline{C}\ \overline{M_x}/(1-\overline{M_x}^2)$ for cut-on modes and $\mathrm{Im}(\lambda_i)$ for cut-off modes, where the overline denotes the mean value of the flow variable over the cross-section. The resulting forward admittance matrix is given by

$$Y_e = W_+^u (W_+^{\phi})^{-1} = W_+^{\phi}\Lambda_+ (W_+^{\phi})^{-1}, \quad (14)$$

where $\Lambda_+ = \mathrm{diag}(\lambda_0, \lambda_1, \lambda_2, ...)$ is the matrix of eigenvalues, and $W_+^\phi = \left(\mathbf{w}_0^\phi, \mathbf{w}_1^\phi, ...\right)$ and $W_+^u = (\mathbf{w}_0^u, \mathbf{w}_1^u, ...)$ are the matrices of potential and axial velocity eigenvectors associated with forward waves. Note that the matrix W_+^ϕ is the transfer matrix from the transverse eigenmode basis to the polynomial basis.

F. Potential calculation

The admittance is calculated from the exit to the source by integrating the equation (12) (the details of this axial integration will be addressed in section III G). Injecting the expression of the admittance into equation (10) gives the following equation for the acoustic potential

$$A_{11}\frac{\mathrm{d}}{\mathrm{d}x}(\boldsymbol{\phi}) = M_{11}\boldsymbol{\phi} + M_{12}Y\boldsymbol{\phi}. \tag{15}$$

It can then be calculated from the source to the exit (more details in section III G). Given an incoming acoustic wave $\boldsymbol{\phi}_s^+$, the potential at the injection is $\boldsymbol{\phi}_s = (I_d + R)\boldsymbol{\phi}_s^+$ with $R = (Y - Y_-)^{-1}(Y_+ - Y)$ the local reflection matrix and $Y_\pm$ the local forward/backward admittance matrix.

G. Modification of the Magnus–Möbius scheme

High-order modes, that are not well captured by the polynomial basis, are present in the calculations when using polynomials for the basis functions, as reported by Wilson et al. 17 and Guennoc et al. 18. Their axial wavenumbers are far from the ones associated with physical modes, and they tend to be strongly cut-off. It will be shown later that the matrices

involved in the Magnus–Möbius scheme are directly related to these wavenumbers. While the physical eigenvalues (obtained when using the hard-wall duct modes as an approximation basis) do not pose a problem, the non-physical eigenvalues obtained when using a polynomial basis lead to poorly conditioned matrices due to their strongly cut-off nature. To avoid this conditioning issue, we propose a modified formulation of the Magnus–Möbius scheme.

Firstly, the classical Magnus–Möbius scheme is as follows. We introduce the exit location x_e and the source position x_s. Considering an axial discretization $(x_n)_{n\in[\![0,N]\!]}$ such that $x_N = x_s$ and $x_0 = x_e$, the potential and acoustic velocity at positions x_n and x_{n+1} are linked using the following equation

$$\begin{pmatrix} \boldsymbol{\phi}_{n+1} \\ \\ \mathbf{u}_{n+1} \end{pmatrix} = \mathrm{e}^{\Omega_n} \begin{pmatrix} \boldsymbol{\phi}_{n} \\ \\ \mathbf{u}_{n} \end{pmatrix}, \tag{16}$$

where the matrix Ω_n is the Magnus matrix, the expression of which can be found using the matrices defined in section III B 14. After splitting the matrix exponential into four blocks

$$\mathrm{e}^{\Omega_n} = \begin{pmatrix} E_1 & E_2 \\ \\ E_3 & E_4 \end{pmatrix}, \tag{17}$$

the evolution of the admittance and the potential are written

$$\begin{aligned} Y_{n+1} &= (E_3 + E_4 Y_n)(E_1 + E_2 Y_n)^{-1} \\ \boldsymbol{\phi}_n &= (E_1 + E_2 Y_n)^{-1} \boldsymbol{\phi}_{n+1}. \end{aligned} \tag{18}$$

The difficulty is that the matrix $(E_1 + E_2 Y_n)$ can be ill-conditioned 18, which makes the scheme not robust for high frequencies or strong flow gradients. We use an eigen decomposition of the matrix Ω_n to avoid using these matrices. Since the transfer matrix $\exp(\Omega_n)$ represents the transfer of information from the axial location x_n to its neighbouring value

188 x_{n+1}, the eigenvalues (Λ_+, Λ_-) of Ω_n, are characteristic of the evolution of right-running
189 $(\boldsymbol{\phi}_+, \mathbf{u}_+)$ and left-running $(\boldsymbol{\phi}_-, \mathbf{u}_-)$ eigenvectors. The exponential matrix can be rewritten
190 as:

$$\mathrm{e}^{\Omega_n} = \begin{pmatrix} \boldsymbol{\phi}_+ & \boldsymbol{\phi}_- \\ \mathbf{u}_+ & \mathbf{u}_- \end{pmatrix} \begin{pmatrix} \mathrm{e}^{\Lambda_+} & 0 \\ 0 & \mathrm{e}^{\Lambda_-} \end{pmatrix} \begin{pmatrix} \boldsymbol{\phi}_+ & \boldsymbol{\phi}_- \\ \mathbf{u}_+ & \mathbf{u}_- \end{pmatrix}^{-1}. \tag{19}$$

191 In addition, by assuming that all the sub-matrices are invertible, the last matrix can be
192 rewritten

$$\begin{pmatrix} \boldsymbol{\phi}_+ & \boldsymbol{\phi}_- \\ \mathbf{u}_+ & \mathbf{u}_- \end{pmatrix}^{-1} = \begin{pmatrix} (\boldsymbol{\phi}_+ - \boldsymbol{\phi}_- \mathbf{u}_-^{-1}\mathbf{u}_+)^{-1} & 0 \\ 0 & (\mathbf{u}_- - \mathbf{u}_+\boldsymbol{\phi}_+^{-1}\boldsymbol{\phi}_-)^{-1} \end{pmatrix} \begin{pmatrix} I_d & -\boldsymbol{\phi}_-\mathbf{u}_-^{-1} \\ -\mathbf{u}_+\boldsymbol{\phi}_+^{-1} & I_d \end{pmatrix}. \tag{20}$$

193 By noting $Y_\pm = \mathbf{u}_\pm\boldsymbol{\phi}_\pm^{-1}$ the admittance matrix associated to respectively right/left run-
194 ning modes, the exponential matrices can be written

$$\begin{aligned} E_1 &= \boldsymbol{\phi}_+\mathrm{e}^{\Lambda_+}\boldsymbol{\phi}_+^{-1}(I_d - Y_-^{-1}Y_+)^{-1} + \boldsymbol{\phi}_-\mathrm{e}^{\Lambda_-}\boldsymbol{\phi}_-^{-1}(I_d - Y_+^{-1}Y_-)^{-1}, \\ E_2 &= \boldsymbol{\phi}_+\mathrm{e}^{\Lambda_+}\boldsymbol{\phi}_+^{-1}(Y_+ - Y_-)^{-1} + \boldsymbol{\phi}_-\mathrm{e}^{\Lambda_-}\boldsymbol{\phi}_-^{-1}(Y_- - Y_+)^{-1}, \\ E_3 &= \mathbf{u}_+\mathrm{e}^{\Lambda_+}\mathbf{u}_+^{-1}(Y_+^{-1} - Y_-^{-1})^{-1} + \mathbf{u}_-\mathrm{e}^{\Lambda_-}\mathbf{u}_-^{-1}(Y_-^{-1} - Y_+^{-1})^{-1}, \\ E_4 &= \mathbf{u}_+\mathrm{e}^{\Lambda_+}\mathbf{u}_+^{-1}(I_d - Y_-Y_+^{-1})^{-1} + \mathbf{u}_-\mathrm{e}^{\Lambda_-}\mathbf{u}_-^{-1}(I_d - Y_+Y_-^{-1})^{-1}. \end{aligned} \tag{21}$$

195 Here the problem associated with the presence of the high-order modes is clearly visible.
196 As these modes are strongly cut-off, the matrices E_1, E_2, E_3, E_4 involve adding terms in
197 e^{Λ_+} to other terms in e^{Λ_-} while these two exponentials have entirely different orders of
198 magnitudes. Depending on the direction of the axial integration, one of those two always
199 corresponds to exponentially increasing terms, say here e^{Λ_+}, while the other is linked to
200 exponentially decreasing terms, say here e^{Λ_-}. This means that the terms in e^{Λ_+} are very

large while the ones in e^{Λ_-} are very small, leading to round-off errors. The goal is to reformulate this expression so as to avoid this summation, which is difficult to compute accurately.

The previous expressions are therefore inserted into the equation (18) to give

$$\begin{aligned} Y_{n+1} &= Y_+ + (Y_- - Y_+)P_- R P_+^{-1}(I_d + P_- R P_+^{-1})^{-1} \\ \boldsymbol{\phi}_n &= (I_d + R)P_+^{-1}(I_d + P_- R P_+^{-1})^{-1}\boldsymbol{\phi}_{n+1}, \end{aligned} \tag{22}$$

where $P_- = \boldsymbol{\phi}_- e^{\Lambda_-}\boldsymbol{\phi}_-^{-1}$, $P_+^{-1} = \boldsymbol{\phi}_+ e^{-\Lambda_+}\boldsymbol{\phi}_+^{-1}$ and $R = (Y_n - Y_-)^{-1}(Y_+ - Y_n)$.

Note that with these expressions, contrary to the ones in (21), there is no summation of the term e^{Λ_+} and e^{Λ_-}. The impact of the high-order mode interaction is included in the term $P_- R P_+^{-1}$, with the high-order modes which are small in both $e^{-\Lambda_+}$ and e^{Λ_-}.

A quick analysis of Y_{n+1} can give us a better understanding of the role of each of the previous matrices. The terms $\boldsymbol{\phi}_\pm e^{\Lambda_\pm}\boldsymbol{\phi}_\pm^{-1}$ are characteristic of the propagation of the left and right running modes between the axial position x_n and x_{n+1}. By analogy to the reflection matrix found when deriving the expression for the potential at the source, the matrix R can be associated with the local reflection between left- and right-running modes. When $Y_n = Y_+$ (constant cross-section duct), $R = 0$ and the formulation reduces to $Y_{n+1} = Y_+$. This is expected because the admittance is constant inside a duct when there is no wall or flow variation. In such a duct $\boldsymbol{\phi}_n = \boldsymbol{\phi}_+ e^{-\Lambda_+}\boldsymbol{\phi}_+^{-1}\boldsymbol{\phi}_{n+1}$ which means that there is also no possible scattering.

Note that the expression obtained for the potential in equation (22) is similar to the ones derived by Wilson 17 or Félix & Pagneux 13, but here we have not neglected the contribution of high-order modes.

Although this methodology is useful, it has two drawbacks. First, computing the eigenvalues of the matrix Ω_n can be numerically costly. Secondly, as explained previously, it is necessary to distinguish between left and right-running modes. Failing to sort these modes correctly can cause some numerical difficulties. In theory, it would be possible to use the group velocity to differentiate between them, but evaluating this term can be challenging in practice. As an alternative, the "transverse-mode" criteria, defined in Section III E, can be used to classify these modes. This method for ordering the different categories of eigenmodes is used in the remainder paper and reliably distinguishes left and right-running modes for the studied cases.

Finally, note that a non-reflective boundary condition at the exit ($R = 0$) becomes available with the newly derived expression. However, it is not used in the remainder of the paper for comparison reasons with validation methodologies and because it causes some phenomena that are not yet explained.

H. Impedance discontinuities

The equation (10) obtained from the multimodal approach is valid as long as the impedance is represented by a differentiable function. However, in practice, the liner is only applied to a finite portion of the duct, which leads to impedance discontinuities. Let us now suppose that one of these discontinuities is located at x_d. We denote x_d^- and x_d^+ the limit when $x \to x_d$ from the left and from the right, respectively. In a previous paper 16, we demonstrated that the jump in the admittance matrix between these two axial locations can be expressed as

$$Y(x_d^-) = \left(\mathcal{A} - \mathcal{N}^-\right)^{-1} \left(\mathcal{P}^- - \mathcal{P}^+ + \left(\mathcal{A} - \mathcal{N}^+\right) Y(x_d^+)\right), \tag{23}$$

with

$$\begin{aligned} \mathcal{A}_{ij} &= \int_S D(1 - M_x^2)\varphi_j \varphi_i^* \mathrm{d}S, \\ (\mathcal{N}^\pm)_{ij} &= \frac{1}{\mathrm{i}\omega} \int_\Lambda \frac{D^2 V_\tau}{Z(x_d^\pm)} U \varphi_j \varphi_i^* \mathrm{d}\Lambda, \\ (\mathcal{P}^\pm)_{ij} &= \frac{1}{\mathrm{i}\omega} \int_\Lambda \frac{D^2 V_\tau}{Z(x_d^\pm)} \left(\mathrm{i}\omega\varphi_j + V \frac{\partial \varphi_j}{\partial r}\right) \varphi_i^* \mathrm{d}\Lambda. \end{aligned} \tag{24}$$

IV. MULTIMODAL FORMULATION FOR FLOW CALCULATIONS

It is interesting to note that solving the acoustic propagation equation (2c) for $\omega \to 0$, $m = 0$ and $\mathbf{V} = \mathbf{0}$ amounts to solving equation (2a) for the potential mean flow, with ϕ replaced by Φ. In this section, we show how to apply the multimodal method developed for acoustic propagation to calculate the mean flow. The same procedure as for the acoustic calculation is followed, but with two important differences, described in the next sections.

A. Iterative procedure

An iterative procedure is required because equation (2a) is non-linear due to the dependence of the mean density D on the velocity potential Φ, as defined by (2b). Starting from an initial value for the density, we solve equation (2c) using the same multimodal method as above to calculate the velocity potential and the axial velocity. A new density field D is then calculated using (2b). This process is repeated until the change in D between two iterations is smaller than a chosen threshold.

B. Inflow condition

The other specificity for using the multimodal method for computing the mean flow lies in the definition of the inflow condition. Indeed, a problem arises when we need to define an admittance at the exit where we consider a constant cross-section duct end. The analogy with the acoustics shows that the first eigenvalue associated with the mean flow potential and mean flow axial velocity is $\lambda = 0$. Equation (14) then indicates that the mean flow potential is not proportional to the mean flow axial velocity. Consequently, the equation (14) cannot be used as such anymore.

To address this limitation, we propose representing the mean flow in constant ducts as a combination of a mean value U_0 and perturbations that vary exponentially. In a constant cross-section duct, the vector of flow axial velocity coefficients is therefore written

$$\mathbf{U}(x) = U_0 \mathbf{w}_0^u + \sum_{i \neq 0} \alpha_i \mathbf{w}_i^u e^{\lambda_i x}, \tag{25}$$

where $\lambda_i \in \mathbb{R}^*$. The term of $\mathbf{w}_0^u$ associated with φ_0 is 1 and all the other ones are equal to zero. This implies that Φ writes

$$\mathbf{\Phi}(x) = U_0 \mathbf{w}_0^\phi + \sum_{i \neq 0} \alpha_i \mathbf{w}_i^\phi e^{\lambda_i x}, \tag{26}$$

where the term of $\mathbf{w}_0^\phi$ associated with the mode φ_0 is $x + cst$. At the exit, this term equals $x_e + cst$.

By noting that the flow perturbations cannot increase in a constant cross-section duct, and therefore by only selecting the eigenvalues associated with exponentially decreasing perturbations, the exit boundary condition for the admittance is

$$Y_e = W_+^u (W_+^\phi)^{-1}. \tag{27}$$

For the flow cases, the admittance matrix plays a double role at the duct exit. On the one hand, it sets the potential constant, and on the other hand, it avoids spurious reflections.

With this value, it is possible to find the admittance everywhere inside the duct using the standard Magnus–Möbius scheme. Unfortunately, the technique to stabilize this scheme for high-order modes cannot be used for the flow since the matrix Ω_n is no more diagonalizable.

Finally, by imposing an "incoming" velocity U_s^+ at the source location and by using the local admittance matrix, it is possible to define an injection condition. The "incoming" velocity is then adjusted to get the desired mass flow.

V. VALIDATION FOR A VARYING DUCT WITH A CIRCULAR CROSS-SECTION

A. Validation methodology

1. Description of the test case

For all the following results, we use the axisymmetric geometry from Reference 28 which is representative of the intake duct of the CFM56 engine. It is entirely defined by the spinner radius R_1 and the radius R_2 of the inner wall of the intake

$$\begin{aligned} R_1(x) &= \max\left(0, 0.64212 - \left(0.04777 + 0.98234\, y^2\right)^{0.5}\right), \\ R_2(x) &= 1 - 0.18453\, y^2 + 0.10158 \frac{\mathrm{e}^{-11(1-y)} - \mathrm{e}^{-11}}{1 - \mathrm{e}^{-11}}, \end{aligned} \tag{28}$$

for $0 \leq x \leq L$ and with $y = x/L$ and $L = 2$. The fan is located at the axial position $x = 0$, and the duct exit at $x = L$. The flow properties are specified at the fan location, with a prescribed axial velocity, density and speed of sound. The density and speed of sound are

set to 1 in all cases of the paper. The acoustic source is defined as an incoming acoustic mode at the fan plane, where the duct has hard walls. This mode is defined by its azimuthal and radial wavenumber orders m and n, respectively. At both ends of the duct, we assume infinite duct conditions with zero reflection coefficients. For test cases with a liner, we apply a constant impedance $Z_2 = 2 - \mathrm{i}$ on the outer wall between $x = 0.2$ and $x = 1.8$.

2. Numerical convergence

For a given two-dimensional variable $f(x, r)$, we define the variables f_p referring to the approximation obtained using the multimodal method with p polynomials. The relative numerical error is defined as

$$\epsilon_p = \left(\frac{\int_{R_1}^{R_2} \int_0^L |f_\mathrm{p} - f_\mathrm{ref}|^2 r \mathrm{d}x\mathrm{d}r}{\int_{R_1}^{R_2} \int_0^L |f_\mathrm{ref}|^2 r \mathrm{d}x\mathrm{d}r} \right)^{1/2}, \tag{29}$$

where f_ref is the reference solution obtained using an FEM code 29 with a fine grid. This FEM code is used to compute both the steady potential flow and the acoustic field. For flow calculations, the error is calculated on the axial velocity, while it is based on the amplitude of complex pressure for acoustic results.

The FEM solutions are computed on an unstructured, triangular mesh generated using Gmsh 30. Quadratic elements (6 node triangles) are used to represent the solutions. To avoid spurious reflections at the inlet and outlet boundary conditions, where a representation over transverse hard-wall modes is used, the duct ends should be located far enough from regions of non-uniformities. Therefore, the duct is extended by straight parts of length 0.5 at the inlet and the outlet to tend to a uniform flow at boundary conditions. The counterpart

is that the sharp junctions between the real duct and the straight duct extensions can also cause reflections, that should nevertheless be captured by the two solvers (note that a non-reflective boundary condition with the original duct geometry could have only been achieved with the multimodal method as discussed at the end of Section III G). A mesh convergence study is performed to evaluate if the acoustic field is accurately represented. When using the FEM solver, there is also a need to refine the mesh near the sharp edges and the liner discontinuities to have an accurate solution.

3. Axial discretization

The multimodal method involves a numerical integration along the x axis, to calculate both the admittance matrix and the sound field. It is important to identify a robust criterion to define the number of points in the axial direction to achieve a trade-off between accuracy and computational efficiency. For this purpose, we follow the approach of Guennoc 18 and define a density, D_{ex}, as the number of points per characteristic length of decay of the most evanescent mode. However, we have to ignore non-physical high-order modes since they are highly evanescent and would lead to a dramatically oversampled mesh. We therefore only consider the first two thirds of the eigenvalues, which is considered to be a good criterion to isolate physical modes 31. If N is the total number of eigenvalues, this means that the discretization is set to correctly capture the axial variation of all modes with a radial order inferior to $2N/3$. In practice, we use the eigenvalues found at the duct exit, λ_i, to define the number of axial grid points N_x

$$N_x = D_{ex}\lambda_{2N/3}L. \tag{30}$$

In the rest of this paper, we use $D_{ex} = 1$ and a second order Magnus–Möbius scheme 14, 19.

B. Flow computation

To validate the computation of the mean flow, three test cases are considered, with a low, medium and high velocity defined at the fan face by $M_s = -0.2$, -0.4 and -0.6, respectively. For each of these cases, the number of Chebyshev polynomials is varied: $p = 3$, 6 or 9. The results are shown in Figure 2. While three polynomials are not sufficient to accurately represent the mean flow, a good representation of the flow can already be achieved with only six polynomials. With nine polynomials, the agreement is excellent. The areas where the accuracy is reduced are near the sharp corners along the duct walls, which are located at the transition from the spinner to the duct axis near $x = 1.25$, and at the exit of the duct $x_e = 2$, where a straight duct is used for the exit condition. At these points, the flow velocity indeed reaches zero to satisfy the zero normal velocity conditions (wall boundary) along the two different normal directions of the sharp corner, which results in strong local gradients in the solution. Yet, these localized losses of accuracy do not impact the rest of the solution, and the method is able to compute the mean flow accurately even with a limited number of polynomials.

The results in Figure 2 also indicate that the required number of polynomials does not depend on the specified Mach number value, since there is no visible loss of accuracy when increasing it. The difference, which is not visible in the graph, is the number of iterations required to converge to the solution of the non-linear equation (2a). For the low-velocity case, only three steps are required to reach a converged solution (with a tolerance of 10^{-5}),

while five steps are needed for the medium-velocity case and seven for the high-velocity case. This is expected, since compressible effects become more significant as the Mach number increases.

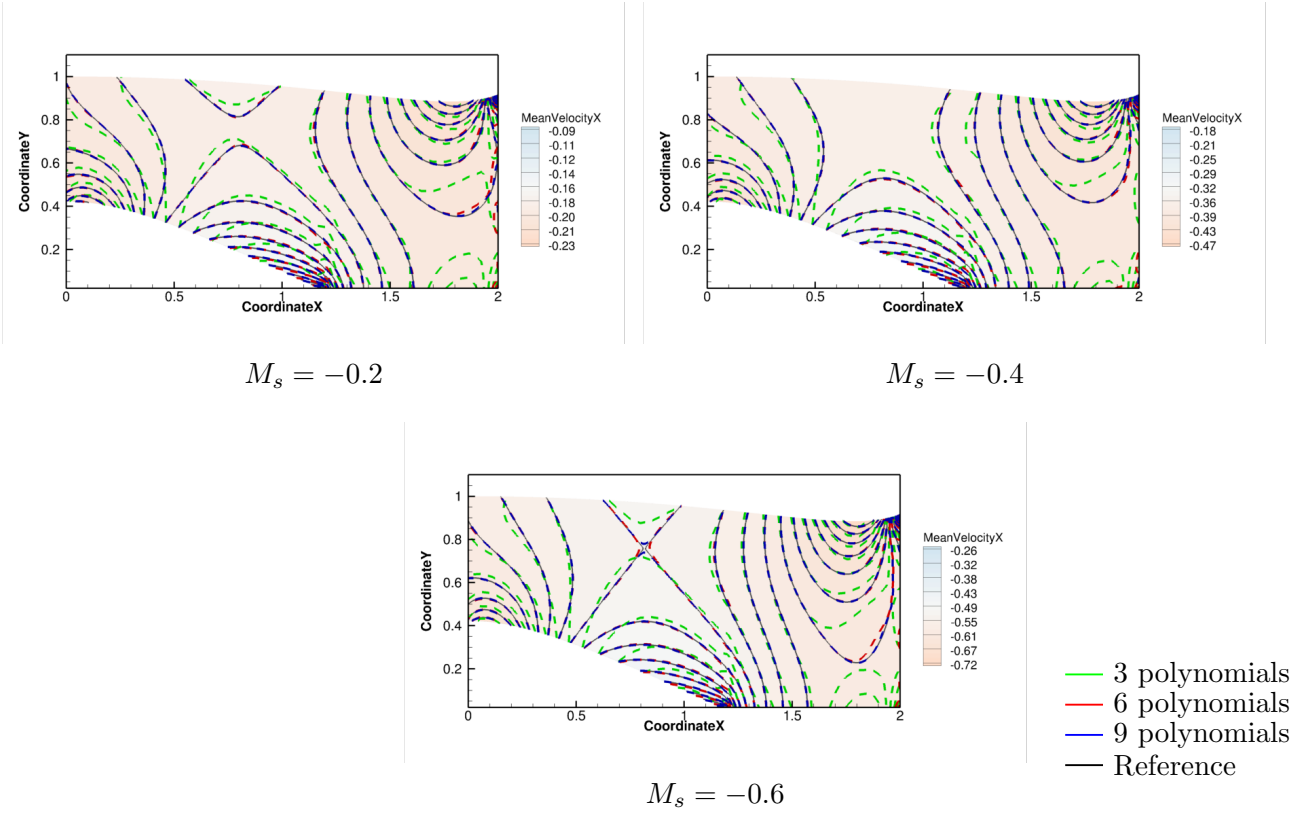

FIG. 2. Contours of normalized axial velocity, overlaid on the reference FEM solution, for varying numbers of polynomials.

Figure 3 presents a convergence analysis using the FEM computations as the reference solutions. The number of polynomials used in the multimodal method is varied between 1 and 50. The results confirm the qualitative observations based on Figure 2. Firstly, an accurate representation of the flow can be obtained even with a small number of polynomials.

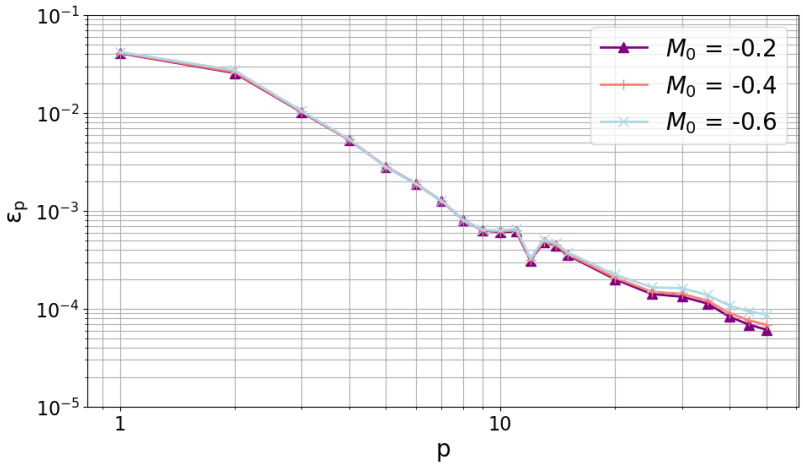

FIG. 3. Relative error on the axial velocity field as a function of the number of polynomials used in the multimodal method and for the three flow velocities.

For example, with just nine polynomials, the relative error is only $\epsilon_p \simeq 6 \times 10^{-4}$. Secondly, the specified Mach number only has a small influence on the accuracy.

To provide an indication of the computational cost of the flow calculations with the multimodal method (based on the Python implementation), we report the CPU time for a single iteration needed to solve Equation (2a). With five polynomials, the time is 0.09 seconds, with ten polynomials it is 0.25 seconds, with twenty polynomials it is 0.97 seconds, and it is 7.2 seconds with fifty polynomials. While the method is advantageous with a small number of polynomials, the calculation time increases rapidly as the number of polynomials increases. Still, the multimodal method can provide useful results with reasonably low computational times.

C. Hard-wall acoustic calculations

The method is designed with high-velocity calculations in mind, since it is precisely in such cases that the multimodal method with a multiple-scale flow presented in a previous paper 16 encounters difficulties. Consequently, the high-velocity flow ($M_s = -0.6$) is used for acoustic computation. Forty polynomials are used for the flow computations to prevent the numerical error on the flow from affecting the acoustic calculations. Note that axial grid points used in the multimodal calculations of the mean flow might differ from those used in the multimodal calculation of the sound field. For this purpose, the amplitudes of the Chebyshev polynomials representing the flow properties are interpolated along the axial direction using a cubic interpolation. The interpolated amplitudes are then used to compute the flow properties at the desired radial locations.

To analyse the acoustic response, we first perform a qualitative test by analyzing contour maps of the sound pressure levels (SPL) defined as

$$p_{SPL} = 20 \log_{10} \left(\frac{|p|}{20 \times 10^{-6}} \right). \tag{31}$$

This is done for a mode $(m, n) = (13, 1)$ at $\omega = 20$ and $\omega = 30$, and for the modes $(m, n) = (1, 1)$ and $(m, n) = (13, 3)$ at $\omega = 20$. These modes include a case where the injected mode encounters a transition from cut-on to cut-off inside the duct ($(m, n) = (13, 3)$) and cases where the injected modes are far from a transition phenomena (all other modes). A unit value is specified for the outer wall pressure of the incoming wave at the source location for all cases. The SPL contours inside the duct are calculated for each case with the FEM,

in order to have a reference solution, and with the multimodal method with various numbers of polynomials $p = 10$, 15 and 25. The results are shown in figure 4.

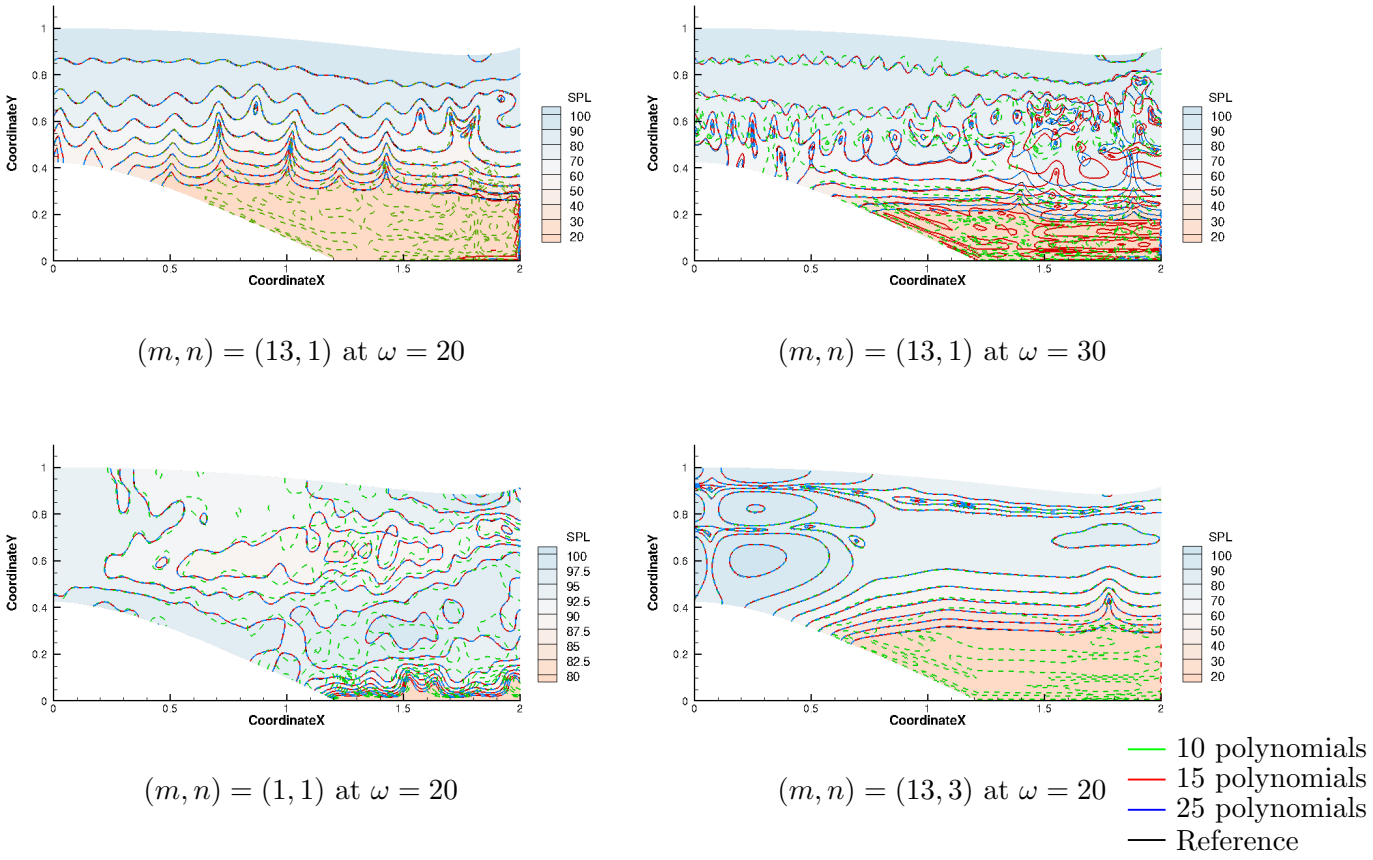

FIG. 4. Contours of sound pressure levels, overlaid on the reference FEM solution, for different numbers of polynomials.

When the mode $(13, 1)$ is injected at $\omega = 20$, even with 10 polynomials, the agreement is already good for SPL between 50 and 110 dB, but the agreement remains poor for low SPL. With 15 or 25 polynomials, the agreement is excellent for all SPL shown in the graph. It should be noted that it is in the regions where the flow speed is higher ($x \in [1.8, 2]$) that the

precision is the lowest. Similar conclusions can be made for the higher radial order mode $(13, 3)$.

When the frequency is increased for the azimuthal mode $(m, n) = (13, 1)$, the agreement is degraded. With 10 polynomials, the pressure field is inaccurate everywhere in the duct. With 15 polynomials, the agreement improves markedly, and for high SPL values, the agreement is acceptable. With 25 polynomials, the agreement is once again excellent. As expected, more polynomials are needed when increasing the frequency since the number of cut-on modes also increases.

To further confirm these qualitative observations, we perform a convergence analysis by plotting, in figure 5, the relative error on the amplitude of acoustic pressure as a function of the number of polynomials. We consider the influence of the azimuthal mode order, the frequency, as well as the first three radial orders. It is important to note that we exclude cases in which the mode is strongly cut-off at the source plane since their strong decay is hard to compute accurately using the FEM.

We first consider the azimuthal mode $m = 1$ for a wide range of polynomials. We observe that the convergence graphs can be divided into three parts for this test case. First, a pre-asymptotic region where the error is almost equal to one and where including further polynomials does not modify the error. Then a sharp decay region, where the convergence is almost exponential (typical of a polynomial basis), is obtained. Lastly, a slower convergence is observed. The authors assume that this last region is linked to the axial discretization, and that the observed convergence rate is related to the order of the Magnus–Möbius scheme. Note that for the pulsation $\omega = 5$, the pre-asymptotic behaviour is not observed mainly

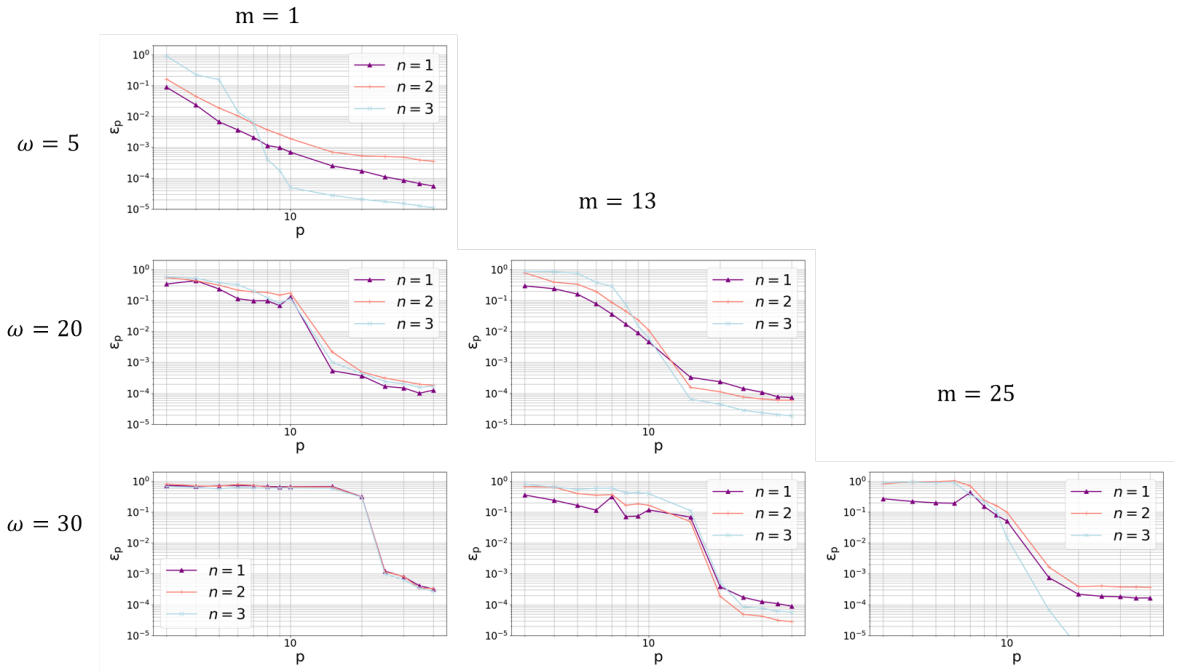

FIG. 5. Relative error on the acoustic pressure amplitude field as a function of the number of polynomials.

because very few polynomials are necessary to accurately represent the acoustic field. For the radial order $n = 3$ of the same frequency, the error decreases more sharply than for the other radial orders for a low number of polynomials $p < 10$, before converging again with the previously observed convergence rates. One explanation for this behaviour is that the Magnus–Möbius scheme is highly adapted to compute cut-off modes. Therefore the convergence rate at the beginning corresponds to the improvement in the representation of the mode $n = 3$. After that, the convergence is more linked to the representation of the modes $n = 1, 2$ (which are cut-on). In fact, the mode $n = 3$ will create modes $n = 1, 2$ by scattering mechanisms. Therefore, the convergence rate after the strong decay is the one of these newly created modes.

When the azimuthal mode increases ($m = 13$ and $m = 25$), all the observations made before remain true except for the size of the pre-asymptotic region. The decrease starts further in the graph since a higher azimuthal mode means that the acoustic energy is mainly concentrated near the tip wall, and higher-order polynomials are necessary to capture it. However, the error remains small even with a limited number of polynomials. In fact, for all frequencies and radial orders, the error is less than 10^{-3} with 30 polynomials.

Next, to assess the effectiveness of the stabilization proposed for the Magnus–Möbius scheme in Section III G, we compare the conditioning of the matrices that need to be inverted for both the standard and improved schemes: namely, $(E_1 + E_2 Y)$ for the standard scheme and $(I_d + P_- R P_+^{-1})$ for the improved scheme. We consider two cases: the mode $(m, n) = (13, 1)$ at $\omega = 20$ and the mode $(m, n) = (1, 1)$ at $\omega = 30$ (both cases use 40 polynomials). The conditioning does not depend on the axial discretization with the modified scheme, while it is highly sensitive to it in the standard scheme. Therefore, to evaluate the improvement brought by the new formulation, four axial integration steps are used with the standard scheme: $D_{ex} = 0.5$, 1, 2, 10. The results are shown in figure 6. As expected, the conditioning of the improved scheme is better than the one of the standard scheme almost everywhere. Some peaks appear in both formulations near axial positions where transition phenomena occur (cut-on to cut-off, or vice versa). For the improved formulation, additional peaks also appear where an error in the sorting of the modes is made. Note that the conditioning of the matrix $(E_1 + E_2 Y)$ is suddenly worsened when the duct cross section goes from annular to circular (around $x = 1.2$). In this region, the proposed stabilized scheme improves the conditioning by several orders of magnitudes.

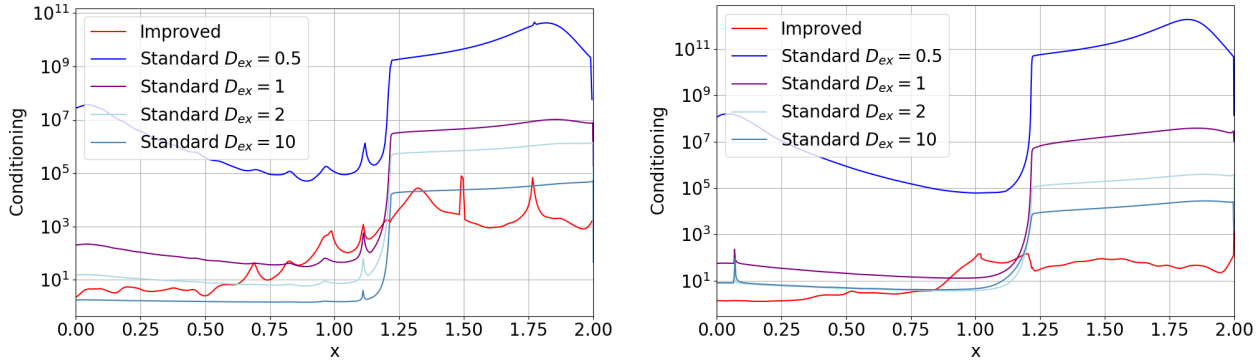

FIG. 6. Conditioning of the matrix to invert in the Magnus-Möbius scheme with the standard and improved formulation.

Finally, we report the computational time required for each calculation. These are measured using a Python implementation of the multimodal method running on a desktop computer. The CPU time is not given for each calculation, but instead we provide a range of runtimes, from the shortest to the longest runtimes for a fixed number of polynomials. With five polynomials, the runtime ranges from 0.02 to 0.9 seconds, while with ten polynomials, it ranges from 0.09 to 3 seconds. Similarly, with twenty polynomials, the runtime ranges from 0.5 to 7 seconds, and with forty polynomials, it ranges from 1.5 to 33 seconds. It is important to note that unlike for the flow calculations in Section V B, the computational time for a given number of polynomials varies significantly depending on the studied mode and frequency since they influence the number of points in the axial direction. Note that the criterion defined for D_{ex} is rather conservative, and sufficiently accurate results can be obtained with smaller values of D_{ex}.

D. Lined acoustic computation

The same test cases are now considered with a lined wall (see section V A 1). It should be recalled that when there is an impedance discontinuity along the wall, the jump condition derived in Section III H is used. In practice, three multimodal computations are done: one before the liner, one in the liner region and the last one after the liner. The admittance jump condition of equation (23) is used between each part. Note that the density criterion D_{ex} is redefined in each region, leading to different axial discretizations. Contours of the sound pressure levels in the duct are given in Figure 7. All the conclusions made for the hard-wall cases remain valid, and an additional observation can be noted. At the junctions between hard and lined walls, the jump in surface impedance induces sharp gradients in the velocity potential, and hence large jumps in the acoustic pressure. This type of weak singularity is difficult to capture with a spectral method 32 such as the multimodal method. It is therefore expected that the rate of convergence of the numerical model will be reduced when compared to the hard-wall test cases. To mitigate this, in the presence of a liner, high-order polynomials are required to accurately represent the large pressure gradients near the end points of the liner. This effect is relatively weak for the first liner discontinuity at $x = 0.2$, but is clearly visible at $x = 1.8$. Two reasons can explain why the effect seems to vary between both discontinuities. First, the fact that there are low SPL values close to the duct axis for the second discontinuity makes the errors more visible. Then, the higher errors at the second discontinuity could also be attributed to the slower convergence of the Chebyshev basis in the circular regions compared to annular ones.

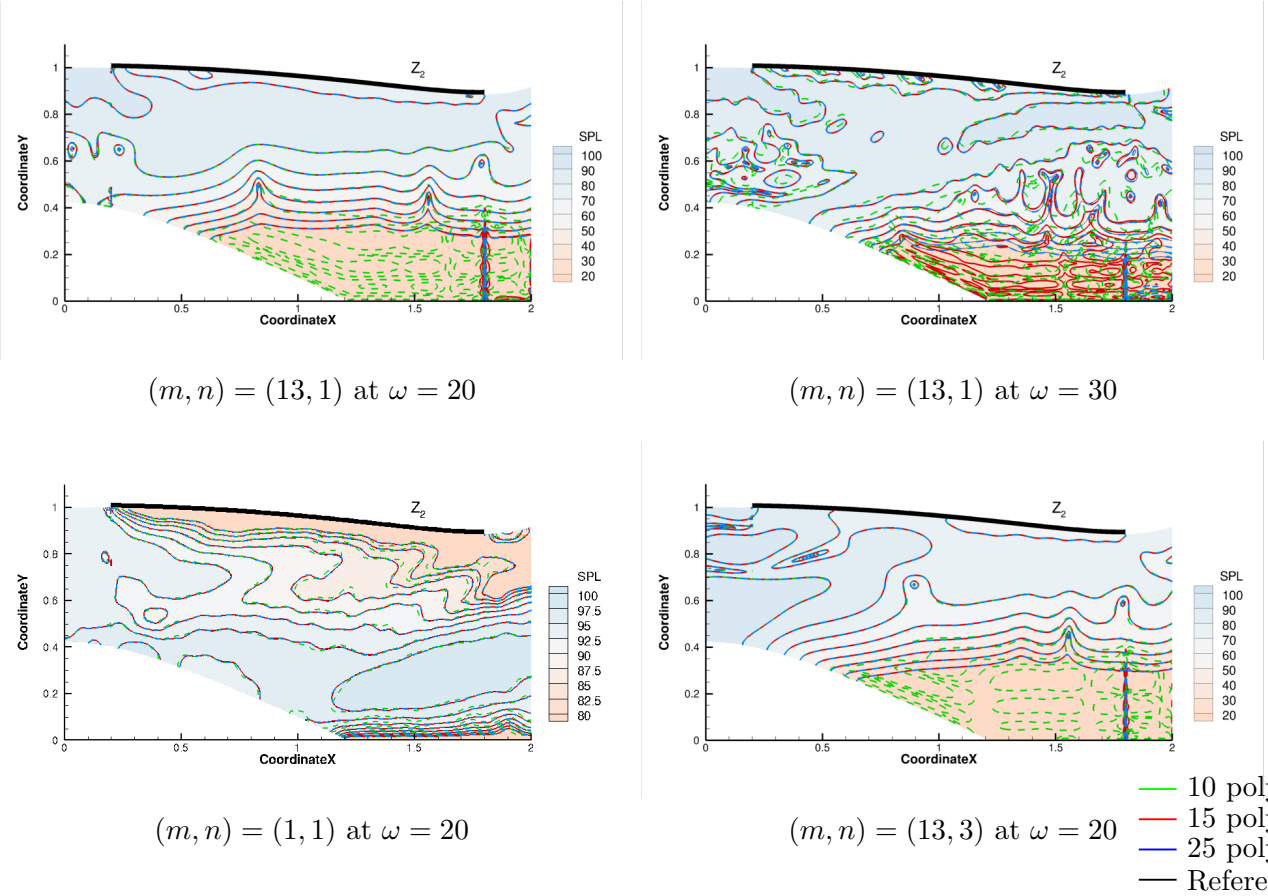

$(m, n) = (13, 1)$ at $\omega = 20$

$(m, n) = (13, 1)$ at $\omega = 30$

$(m, n) = (1, 1)$ at $\omega = 20$

$(m, n) = (13, 3)$ at $\omega = 20$

FIG. 7. Contours of the sound pressure level in the lined duct, overlaid on the reference FEM solution, for different numbers of polynomials.

Once again, a convergence study is performed, and the same flow condition and acoustic modes as the ones used for the hard-wall validation are taken. Figure 8 presents the results. As expected, achieving a precision of 10^{-3} requires more polynomials than the hard-wall case, and the convergence rate is lower. This slower convergence rate makes the method less appealing for lined wall computations. It would be necessary to add supplementary modes to address the singularities in the pressure field and avoid this slow convergence. Another key observation is that the liner tends to smooth the convergence plots by decreasing the size of the pre-asymptotic region, and for the most difficult hard-wall cases ($\omega = 30$), the

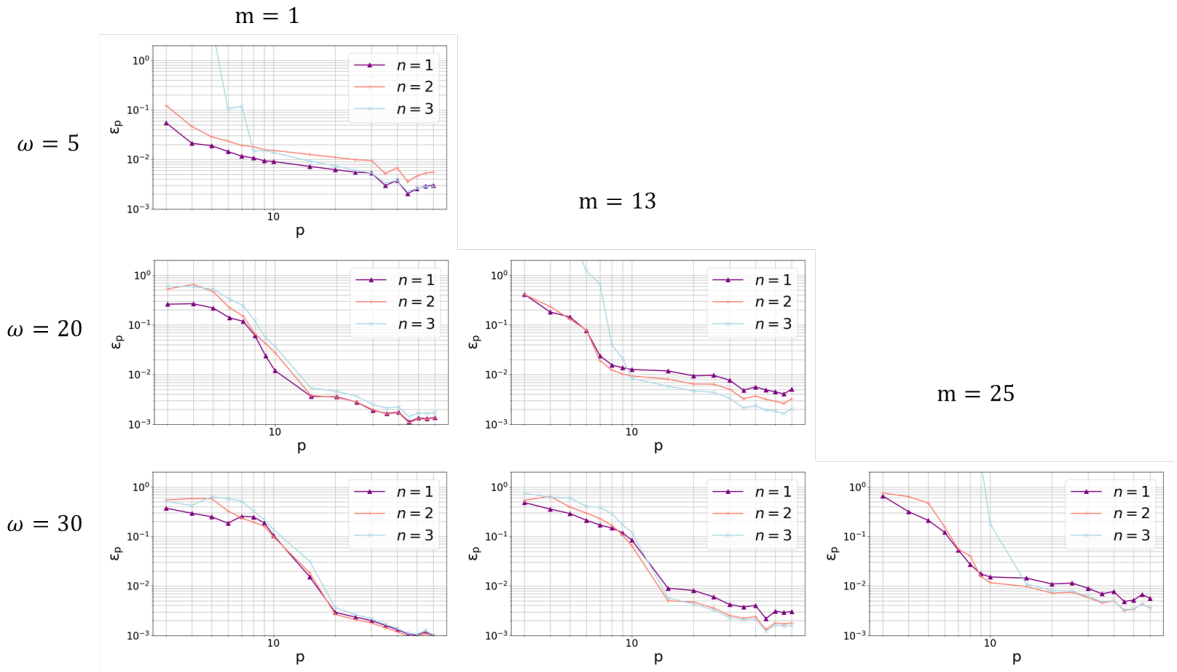

FIG. 8. Relative error on the acoustic pressure amplitude field as a function of the number of polynomials for the lined duct cases.

error goes faster to a value of 10^{-2}. This could be due to the fact that the method captures well the attenuation of the liner with few polynomials ($p < 20$), even if the prediction of the pressure singularity is erroneous. These singularities also pose problems with finite element methods, where it is necessary to refine the region around them. Note that the calculation times required by the multimodal method are similar to the ones obtained for the hardwalled test cases.

VI. CONCLUSION

This paper presents a novel multimodal method to efficiently compute the acoustic field in a duct with a potential mean flow. The acoustic potential equation is rearranged into a

system with only first-order derivatives in the axial direction governing the evolution of the acoustic potential and acoustic axial velocity. Fourier functions and Chebyshev polynomials provide the approximation basis in the duct cross-section, while a Magnus–Möbius scheme is used to integrate the equations in the axial direction. The use of a high-order polynomials basis results in the presence of spurious, non-physical modes. This is a problem common to multimodal schemes using polynomial bases, and is not related to the presence of a mean flow. A modification of the Magnus–Möbius scheme is proposed to avoid the poor conditioning associated with the spurious modes. Results demonstrate that this modification of the integration scheme significantly improves the conditioning of the model. Consequently, larger axial steps can be used for Magnus–Möbius scheme, hence reducing the computational cost of the method. This method, initially devoted to acoustics, has been, in addition, adapted to compute the potential mean flow required for acoustic computations by modifying the boundary conditions and applying an iterative method to solve the non-linear flow equation.

The proposed method has been compared against a finite-element method on a model of a turbofan inlet with hard and lined walls for several frequencies and modes. Validation test cases demonstrate excellent agreement between the multimodal method and the FEM solutions when a sufficient number of polynomials is used. For the mean flow, the proposed method provides quick and accurate results, even for high flow velocities and a number of polynomials as low as 9. For acoustic propagation with hard-wall conditions, a relative error smaller than 10^{-3} can be achieved for all cases with only 25 polynomials, resulting in very short computational times. However, for cases with lined ducts, the presence of

strong gradients in the solutions near impedance discontinuities requires the use of more polynomials to achieve a similar level of accuracy. The computational cost therefore increases for lined ducts, but the method remains efficient compared to a traditional finite-element model.

While validations were conducted on axisymmetric ducts and flows, the method is also applicable to non-axisymmetric flows, but it would require solving the acoustic equation for several azimuthal orders simultaneously since these are coupled together. It would be interesting to use this method to study phenomena such as flow distortion generated by an angle of incidence into a turbofan intake.

APPENDIX A: MULTIMODAL MATRICES

The detailed expressions for the matrices introduced in the multimodal method are as follows

$$
\begin{aligned}
(A_{11})_{ij} &= \int_S D(1-M_x^2)\varphi_j\varphi_i^* \mathrm{d}S, \\
(A_{12})_{ij} &= 0, \\
(A_{21})_{ij} &= -\int_S \frac{DU}{C^2}\frac{\mathrm{D}_\perp\varphi_j}{\mathrm{D}t}\varphi_i^*\mathrm{d}S - \frac{1}{\mathrm{i}\omega}\int_\Lambda \frac{D^2V_\tau}{Z}\frac{\mathrm{D}_\perp\varphi_j}{\mathrm{D}t}\varphi_i^*\mathrm{d}\Lambda, \\
(A_{22})_{ij} &= \int_S D(1-M_x^2)\varphi_j\varphi_i^*\mathrm{d}S - \frac{1}{\mathrm{i}\omega}\int_\Lambda \frac{D^2V_\tau U}{Z}\varphi_j\varphi_i^*\mathrm{d}\Lambda, \\
(M_{11})_{ij} &= -\int_S D(1-M_x^2)\frac{\partial\varphi_j}{\partial x}\varphi_i^*\mathrm{d}S, \\
(M_{12})_{ij} &= \int_S D(1-M_x^2)\varphi_j\varphi_i^*\mathrm{d}S, \\
(M_{21})_{ij} &= \frac{\mathrm{d}}{\mathrm{d}x}\left(\int_S \frac{DU}{C^2}\frac{\mathrm{D}_\perp\varphi_j}{\mathrm{D}t}\varphi_i^*\mathrm{d}S\right) + \int_S D\nabla_\perp\varphi_i^*\cdot\nabla_\perp\varphi_j\mathrm{d}S \\
&\quad - \int_S \frac{D}{C^2}\left(\frac{\mathrm{D}_\perp\varphi_j}{\mathrm{D}t}\left(\frac{\mathrm{D}_\perp\varphi_i}{\mathrm{D}t}\right)^* + U\frac{\mathrm{D}_\perp\varphi_j}{\mathrm{D}t}\frac{\partial\varphi_i^*}{\partial x}\right)\mathrm{d}S \\
&\quad - \frac{1}{\mathrm{i}\omega}\int_\Lambda \frac{D^2}{Z}\frac{\mathrm{D}_\perp\varphi_j}{\mathrm{D}t}\left(\frac{\mathrm{D}\varphi_i}{\mathrm{D}t}\right)^*\mathrm{d}\Lambda + \frac{1}{\mathrm{i}\omega}\frac{\mathrm{d}}{\mathrm{d}x}\left(\int_\Lambda \frac{D^2V_\tau}{Z}\frac{\mathrm{D}_\perp\varphi_j}{\mathrm{D}t}\varphi_i^*\mathrm{d}\Lambda\right), \\
(M_{22})_{ij} &= -\frac{\mathrm{d}}{\mathrm{d}x}\left(\int_S D(1-M_x^2)\varphi_j\varphi_i^*\mathrm{d}S\right) \\
&\quad + \int_S D(1-M_x^2)\varphi_j\frac{\partial\varphi_i^*}{\partial x}\mathrm{d}S - \int_S \frac{DU}{C^2}\varphi_j\left(\frac{\mathrm{D}_\perp\varphi_i}{\mathrm{D}t}\right)^*\mathrm{d}S \\
&\quad - \frac{1}{\mathrm{i}\omega}\int_\Lambda \frac{D^2}{Z}U\varphi_j\left(\frac{\mathrm{D}\varphi_i}{\mathrm{D}t}\right)^*\mathrm{d}\Lambda + \frac{1}{\mathrm{i}\omega}\frac{\mathrm{d}}{\mathrm{d}x}\left(\int_\Lambda \frac{D^2V_\tau U}{Z}\varphi_j\varphi_i^*\mathrm{d}\Lambda\right).
\end{aligned}
$$

Acknowledgments

ONERA carried out these activities in the framework of the ADEC project. This project has received funding from the Clean Sky 2 Joint Undertaking within the European Union's

Horizon 2020 research and innovation program, under grant agreement GA ID No. 945583 - LPA IADP 2020-2021.

Author Declarations

The authors declare no competing interests. The data that support the findings of this study are available within the article.

References

[1]S. Redonnet, E. Manoha, and P. Sagaut, "Numerical simulation of propagation of small perturbations interacting with flows and solid bodies," in *7th AIAA/CEAS Aeroacoustics Conference and Exhibit* (2001), doi: mu10.2514/6.2001-2223.

[2]S. Redonnet and Y. Druon, "Computational aeroacoustics of aft fan noises characterizing a realistic coaxial engine," AIAA Journal **50**(5), 1029–1046 (2012) doi: mu10.2514/1.J050730.

[3]S. Redonnet and G. Cunha, "An advanced hybrid method for the acoustic prediction," Advances in Engineering Software **88**, 30–52 (2015) doi: mu10.1016/j.advengsoft.2015.05.006.

[4]M. C. Duta and M. B. Giles, "A three-dimensional hybrid finite element/spectral analysis of noise radiation from turbofan inlets," Journal of Sound and Vibration **296**(3), 623–642 (2006) doi: mu10.1016/j.jsv.2006.03.006.

[5]I. Achunche, J. Astley, R. Sugimoto, and A. Kempton, "Prediction of forward fan noise propagation and radiation from intakes," 15th AIAA/CEAS Aeroacoustics Conference (30th AIAA Aeroacoustics Conference) (2009) doi: mu10.2514/6.2009-3239.

[6]R. J. Astley, R. Sugimoto, and P. Mustafi, "Computational aero-acoustics for fan duct propagation and radiation. Current status and application to turbofan liner optimisation," Journal of Sound and Vibration **330**(16), 3832–3845 (2011) doi: mu10.1016/j.jsv.2011.03.022.

[7]A. G. Prinn, R. Sugimoto, and R. J. Astley, "The effect of steady flow distortion on noise propagation in turbofan intakes," 22nd AIAA/CEAS Aeroacoustics Conference, 2016 (2016) doi: mu10.2514/6.2016-3028.

[8]S. W. Rienstra, "Sound transmission in slowly varying circular and annular lined ducts with flow," Journal of Fluid Mechanics **380**, 279–296 (1999) doi: mu10.2514/6.1998-2311.

[9]N. Peake and A. J. Cooper, "Acoustic propagation in ducts with slowly varying elliptic cross-section," Journal of Sound and Vibration **243**(3), 381–401 (2001) doi: mu10.1006/jsvi.2000.3411.

[10]N. C. Ovenden, "A uniformly valid multiple scales solution for cut-on cut-off transition of sound in flow ducts," Journal of Sound and Vibration **286**(1-2), 403–416 (2005) doi: mu10.1016/j.jsv.2004.12.009.

[11]R. P. Dougherty, "A parabolic approximation for flow effects on sound propagation in nonuniform, softwall, ducts," in *5th AIAA/CEAS Aeroacoustics Conference* (1999), doi: mu10.2514/6.1999-1822.

[12]V. Pagneux, N. Amir, and J. Kergomard, "A study of wave propagation in varying cross-section waveguides by modal decomposition. Part I. Theory and validation," The Journal of the Acoustical Society of America **100**(4), 2034 (1996) doi: mu10.1121/1.417913.

[13]S. Félix and V. Pagneux, "Multimodal analysis of acoustic propagation in three-dimensional bends," Wave Motion **36**(2), 157–168 (2002) doi: mu10.1016/S0165-2125(02)00009-4.

[14]V. Pagneux, "Multimodal admittance method in waveguides and singularity behavior at high frequencies," Journal of Computational and Applied Mathematics **234**(6), 1834–1841 (2010) doi: mu10.1016/j.cam.2009.08.034.

[15]T. Guennoc, J. B. Doc, and S. Félix, "Improved multimodal formulation of the wave propagation in a 3D waveguide with varying cross-section and curvature," The Journal of the Acoustical Society of America **149**(1), 476–486 (2021) doi: mu10.1121/10.0003336.

[16]B. Mangin, M. Daroukh, and G. Gabard, "Propagation of Acoustic Waves in Ducts with Flow Using the Multimodal Formulation," AIAA Journal **61**(6) (2023) doi: mu10.2514/1.J062659.

[17]A. Wilson, "Propagation of acoustic perturbations in non-uniform ducts with non-uniform mean flow using eigen analysis in general curvilinear coordinate systems," Journal of Sound and Vibration **443**, 605–636 (2019) doi: mu10.1016/j.jsv.2018.11.023.

[18]T. Guennoc, "Modélisation du rayonnement des guides de forme complexe par une méthode multimodale," Ph.D. thesis, Le Mans Université, 2021.

[19]Y. Y. Lu, "A fourth-order Magnus scheme for Helmholtz equation," Journal of Computational and Applied Mathematics **173**(2), 247–258 (2005) doi: mu10.1016/j.cam.2004.03.010.

[20]M. K. Myers, "On the acoustic boundary condition in the presence of flow," Journal of Sound and Vibration **71**(3), 429–434 (1980) doi: mu10.1016/0022-460X(80)90424-1.

[21]W. Eversman, "The boundary condition at an impedance wall in a non-uniform duct with potential mean flow," Journal of Sound and Vibration **246**(1), 63–69 (2001) doi:

601 mu10.1006/jsvi.2000.3607.

602 [22]J. P. McTavish and E. J. Brambley, "Nonlinear sound propagation in two-dimensional
603 curved ducts: A multimodal approach," Journal of Fluid Mechanics **875**, 411–447 (2019)
604 doi: mu10.1017/jfm.2019.497.

605 [23]J. F. Mercier and A. Maurel, "Improved multimodal method for the acoustic propagation
606 in waveguides with a wall impedance and a uniform flow," Proceedings of the Royal Society
607 A: Mathematical, Physical and Engineering Sciences **472** (2016) doi: mu10.1098/rspa.
608 2016.0094.

609 [24]C. Canuto, M. Y. Houssanini, A. Quarteroni, and T. A. Zang, *Springer series in compu-*
610 *tational physics* (Springer, New York, 1988).

611 [25]E. J. Brambley and N. Peake, "Sound transmission in strongly curved slowly varying
612 cylindrical ducts with flow," Journal of Fluid Mechanics **596**, 387–412 (2008) doi: mu10.
613 1017/S0022112007009603.

614 [26]G. Boyer, E. Piot, and J. P. Brazier, "Theoretical investigation of hydrodynamic surface
615 mode in a lined duct with sheared flow and comparison with experiment," Journal of
616 Sound and Vibration **330**(8), 1793–1809 (2010) doi: mu10.1016/j.jsv.2010.10.035.

617 [27]H. Ralph Lewis and P. M. Bellan, "Physical constraints on the coefficients of Fourier
618 expansions in cylindrical coordinates," Journal of Mathematical Physics **31**(11), 2592–
619 2596 (1990) doi: mu10.1063/1.529009.

620 [28]N. C. Ovenden, W. Eversman, and S. W. Rienstra, "Cut-on cut-off transition in flow ducts:
621 comparing multiple-scales and finite-element solutions," in *10th AIAA/CEAS Aeroacous-*

tics Conference (2004), doi: mu10.2514/6.2004-2945.

[29]G. Gabard, "PFE Software" (2021), muhttps://github.com/GwenaelGabard/pfe.

[30]C. Geuzaine and J. F. Remacle, "Gmsh: A 3-D finite element mesh generator with built-in pre-and post-processing facilities," International journal for numerical methods in engineering **79**(11), 1309–1331 (2009) doi: mu10.1002/nme.2579.

[31]A. J. Cooper and N. Peake, "Propagation of unsteady disturbances in a slowly varying duct with mean swirling flow," Journal of Fluid Mechanics **445**, 207–234 (2001) doi: mu10.1017/s0022112001005559.

[32]J. P. Boyd, *Chebyshev and Fourier Spectral Methods*, 2nd ed., rev ed. (Springer Berlin Heidelberg, Mineola, N.Y, 1989).